Manufacturing Letters 26 (2020) 29–32

Contents lists available at ScienceDirect

Manufacturing Letters

journal homepage: www.elsevier.com/locate/mfglet

Letters

Enumeration of additive manufacturing toolpaths using Hamiltonian paths

Puikei Cheng [a,b], Wing Kam Liu [a], Kornel Ehmann [a], Jian Cao [a,*]

[a] Department of Mechanical Engineering, Northwestern University, Evanston, IL 60208, United States
[b] Exponent, Chicago, IL 60661, United States

ARTICLE INFO

Article history:
Received 4 December 2019
Received in revised form 9 September 2020
Accepted 13 September 2020
Available online 7 October 2020

Keywords:
Graph theory
Toolpath
Additive manufacturing
Cooling rates
Microstructure

ABSTRACT

Toolpath choice in metal-based additive manufacturing (AM) affects local thermal environment. We use Hamiltonian paths to systematically enumerate time- and space-continuous toolpaths on example $n \times n$ grid geometries. This framework broadens the toolpath design space by establishing a finite and searchable number of AM toolpaths for any discretized geometry. We characterize toolpaths by extracting toolpath internal structures, e.g., the number of corners and pairs of parallel tracks. The enumerated toolpaths serve as an input to thermal simulations to obtain solidification cooling rate statistics, which strongly correlate to the number of internal structures. Hence, toolpath can be linked to microstructural predictions.

1. Introduction

Additive manufacturing (AM) allows for the design of process parameters and part properties. Unlike in traditional manufacturing, the pointwise thermal histories of a metal-based additive manufactured part differ widely within small spatial scales. Local variability in thermal histories leads to local variability in the microstructure and mechanical properties [1], so resultant microstructures and properties are spatially heterogeneous even if global processing parameters such as laser power or speed remain constant [2,3].

Toolpaths define the pointwise material activation order in time and space, and therefore introduces great variability to the AM process. Three common space-continuous toolpaths (with 2D cross-section, solid infill) are the bi-directional raster (serpentine), offset (spiral), and fractal (crimped) patterns [2]. Although raster patterns are easier to implement, spiral and crimped patterns produce less part distortion and cracking [4–6]. Toolpath also affects residual stress distribution and mechanical properties [7,8]. Attempts to optimize toolpaths often focus on accommodating complex cross-section geometries [9,10] or assume pre-selected patterns for each "island" [11].

The toolpath design space is much larger than the common patterns mentioned above. Generating irregular toolpaths widens the search space to enable better process parameter optimization. Here, we show a general algorithm for enumerating AM toolpaths on discretized geometries. We characterize these toolpaths based on their internal structures and build multiple linear regression models to evaluate their impact on thermal history attributes.

2. Methodology: Hamiltonian path algorithms for generating AM toolpaths

A geometric object with finite volume can be discretized into a finite number of sub-volumes, e.g. by mesh generation into elements. The AM build process requires that each sub-volume of the given geometry be activated exactly once by the heat source. Thus, for a discretized geometry with n sub-volumes, there is a maximum of $n!$ activation sequences. Since the number of permutations of a finite set is finite, the number of AM toolpaths for a specific geometric discretization has an upper bound. By modeling a toolpath as permutations of activated sub-volumes, we expand the toolpath design space to a much larger yet finite and countable number of toolpaths. To minimize build time and melt pool instabilities [12], this study is limited to space- and time-continuous toolpaths, e.g., no jumps in space nor dwell times.

To enumerate space- and time-continuous AM toolpaths, we find an equivalent algorithm in graph theory. The problem of generating AM toolpaths on a discretized geometry is equivalent to that of generating Hamiltonian paths on a graph. In graph theory, paths are a sequence of distinct edges connecting a sequence of

* Corresponding author.
E-mail address: jcao@northwestern.edu (J. Cao).

https://doi.org/10.1016/j.mfglet.2020.09.008

distinct vertices. A Hamiltonian path visits each vertex of the graph once. By representing the target discretized geometry as a graph, where each vertex represents a sub-volume and each edge connects pairs of neighboring sub-volumes, we use established backtracking Hamiltonian pathfinding algorithms to enumerate AM toolpaths. Fig. 1 shows examples of discretized geometries, graphs, and Hamiltonian paths. Our toolpath enumeration process produces a data set of toolpaths. For practicality, the dimensions of the discretized sub-volumes are assumed equal to a constant melt pool track width and height.

For demonstration, we chose grids of $n \times n$ square sub-volumes to verify the toolpath enumeration algorithm. The number of toolpaths generated matches the theoretical number of directed Hamiltonian paths on an $n \times n$ grid graph [13]. Because of rotational and reflectional symmetries in square geometries, the number of unique toolpaths for square grids reduces by a factor of eight. Each toolpath is encoded as a sequence of vertices of length $n \times n$, which is the number of sub-volumes in the discretized geometry.

3. Toolpath internal structures for thermal attribute prediction

The number of possible toolpaths grows with the geometry size. To describe irregular toolpaths, we establish quantitative measures for characterization. We find that internal structures such as L-turns, U-turns, and parallel/antiparallel pairs of straight tracks can be used to characterize toolpaths. L-turns are 90° corners in the toolpath; U-turns are two subsequent left or right L-turns. Parallel tracks are adjacent tracks with the heat source traveling in the same direction, whereas antiparallel tracks are of opposing directions. These toolpath internal structures affect the local thermal environment of AM builds; for example, melt pools are more stable in the middle of tracks than at turning ends because instabilities occur at velocity changes [14,15], leading to keyhole pore formation [16]. Our hypothesis is that if two toolpaths have similar internal structures, their thermal histories and properties may be similar as well.

We use contact maps [17,18] as a tool for quantifying internal structures. In our 2D regular grid geometry, each vertex i has four neighboring vertices. The corresponding contact map records each pair of neighboring vertices, i and j, as an entry in row i column j. Because of symmetry, only the upper triangular matrix is needed. Each toolpath has a unique contact map representation; three common toolpaths and their corresponding contact maps are illustrated in Fig. 2. Patterns formed in the contact map correspond to the aforementioned internal structures of interest, which are identified and counted from the contact map using 8-way connected-region labeling [19] in OpenCV [20].

Multiple linear regression will be used to find correlations between the number of internal structures and their effect on thermal attributes. To generate thermal attributes, we performed transient thermal simulations of single-layer 5x5 square plates built by a Directed Energy Deposition (DED), a powder-blown AM process. The process parameters of track width and height, laser radius, speed, and power are taken from [21], which are 3 *mm*, 0.5 *mm*, 1.75 *mm*, 1000 *mm*/*min*, and 2000 *W*, respectively. The build was resolved with a $40 \times 40 \times 5$ mesh. Material properties of Inconel 625 and finite element solver details are found in [22]. Each simulation takes a toolpath as input and outputs the 4D thermal history within the build. Velocity changes are assumed to be near-instantaneous.

Our chosen thermal attribute for analysis is the Solidification Cooling Rate (SCR), which is linked to microstructural distribution such as porosity and dendrite spacing [23,24]. Higher cooling rates cause finer grain microstructures [25]. SCR is a local scalar variable calculated using:

$$SCR = \left|\frac{T_L - T_S}{t_L - t_S}\right| \tag{2}$$

where T_L and T_S, and t_L and t_S are the temperatures and times at liquidus and solidus, respectively, at a time resolution of 1e-4*s*. We aggregate SCR data for each build by calculating the arithmetic mean and the fraction of SCR outliers according to the interquartile rule for outliers. For our data set, SCR values above 2140 [*K*/*s*] are considered outliers. Because cooling rate is the product of thermal gradient and solidification front velocity [26], toolpaths with higher SCR mean will have finer average grain sizes. Toolpaths with higher SCR outlier fractions may have larger populations of defects or regions of ultra-fine grains.

4. Results and discussion

Multiple linear regression analysis was used to study the impact of toolpath internal structures on SCR statistics. The chosen internal structures are the numbers of L-turns and U-turns, and the numbers of sub-volumes participating in parallel and antiparallel tracks (i.e., total length). The chosen SCR statistics are SCR mean and outlier fraction. To prevent overfitting, each instance of the model was trained on a randomly-selected 70% of the total data; the regression analysis was repeated 100 times. Both predictor and response variables were standardized using z-scores.

Table 1 shows the model results. The low p-values indicate significance in the impact of the internal structures on SCR statistics. The R^2 values indicate that the internal structures are strongly correlated to SCR mean and weakly correlated to outlier fraction, also suggesting that SCR mean is only loosely correlated to the outlier fraction. This demonstrates a need for models and parameters that capture the behavior of extreme values and inhomogeneity.

The standardized regression coefficients reveal a negative correlation between internal structures and SCR statistics. For example, the number of L-turns is the strongest predictor of SCR statistics. This is because corner structures in the toolpath tend to concentrate heat in localized regions and prevent material from cooling off between neighboring depositions. Conversely, straight

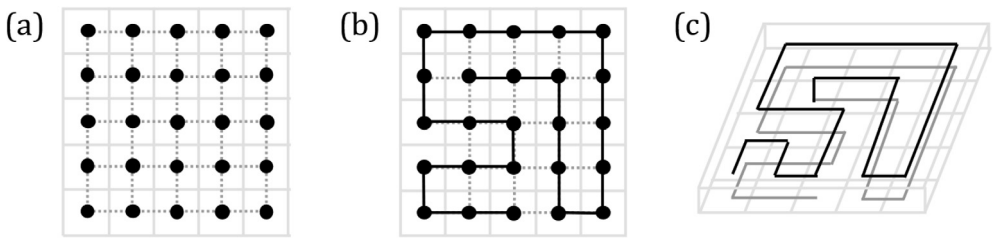

Fig. 1. (a) A single-layer square geometry can be represented by a 5×5 grid graph, where each sub-volume is represented by a graph vertex and four neighboring sub-volumes are connected by edges (in dashed lines). Examples of Hamiltonian paths on (b) a 5×5 grid graph and (c) a $5 \times 5 \times 2$ grid graph (in solid lines) shows that this concept is extendible to multi-layer builds. For the 5×5 grid geometry, there are 1081 toolpaths each of length 25.

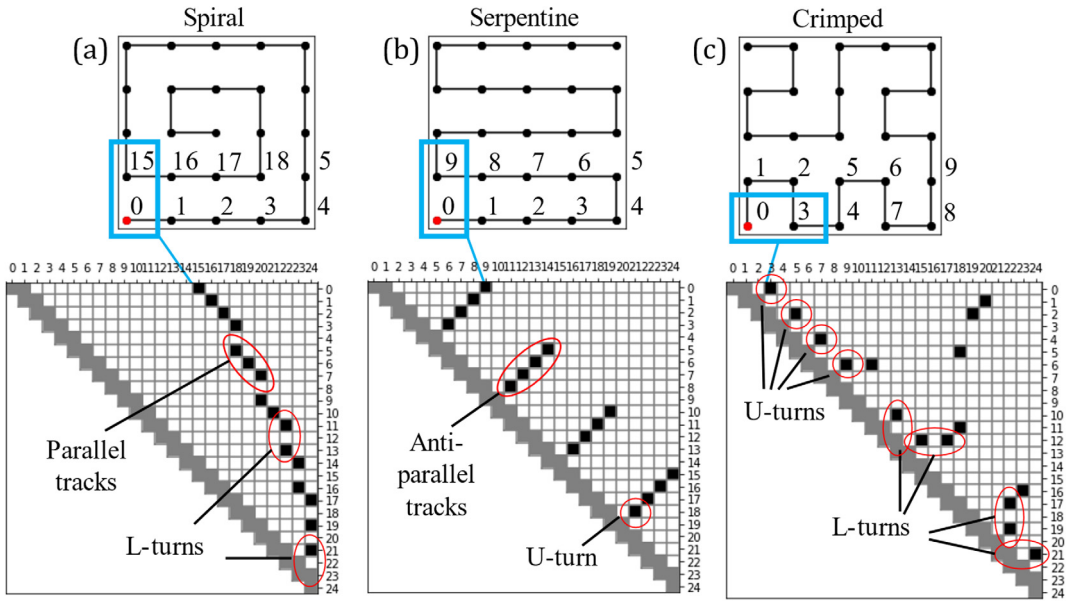

Fig. 2. Common toolpaths (a) spiral, (b) serpentine, and (c) crimped, with their associated contact maps. In these three toolpaths, node 0 is neighbor to, or adjacent to, nodes 15, 9, and 3 in subfigures a-c, respectively. Adjacency is marked as entries in the corresponding columns in row 0 in the contact maps. Diagonal lines with negative slope correspond to pairs of parallel tracks; diagonal lines with positive slope to antiparallel tracks. L-turns correspond to pairs of entries separated by one unit of distance, whereas U-turns correspond to single-entries on the order 3 diagonal.

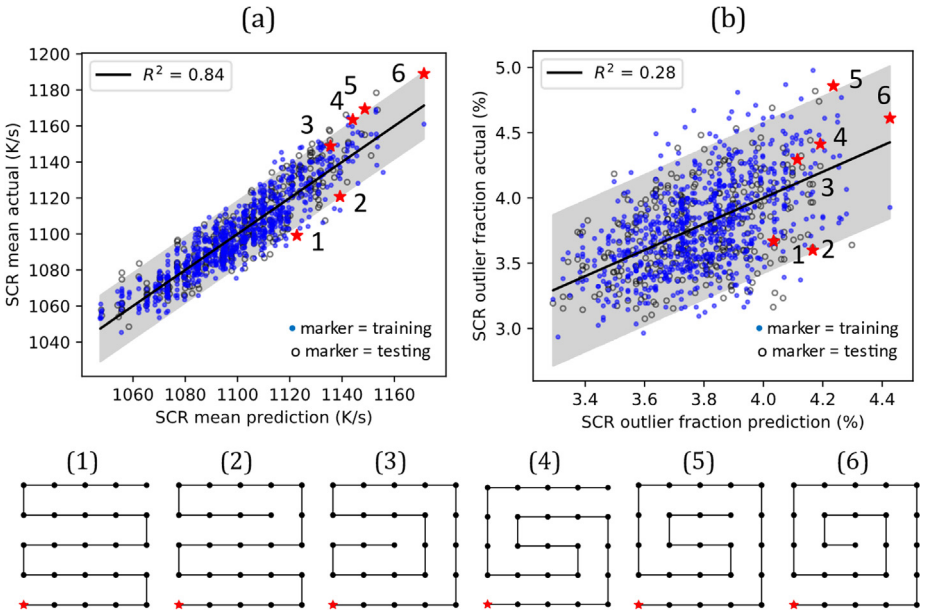

Fig. 3. (a) SCR mean and (b) SCR outlier fraction calculated from simulations vs. as predicted by one instance of the multiple linear regression model. Each point on the scatter plot represents a toolpath. Toolpaths of interest are highlighted in the regression results and visualized (1–6).

Table 1
Average multiple linear regression model standardized coefficients, intercept, and R^2 values for models of SCR statistics (mean and outlier fraction) vs toolpath internal structures, collected over 100 runs of the model, each run trained on 70% of the total data set.

		Predictor variables					
Response variables		L-turns	U-turns	Parallel tracks length	Antiparallel tracks length	Intercept	R^2
SCR mean [K/s]	Mean standardized coefficient (β)	−20.2	−9.92	−6.98	−14.6	1100	0.84
	Mean p-value	<0.001	<0.001	<0.001	<0.001		
SCR outlier fraction [%]	Mean standardized coefficient (β)	−45.0	−19.3	−8.69	−23.7	3.85	0.28
	Mean p-value	1.64e-3	0.0578	0.769	0.0669		

track structures (especially parallel tracks) increase the likelihood of depositing next to cooled material, resulting in higher thermal mismatch, higher SCR, and finer grains. These cooling rates will also impact the residual stresses in the build.

Fig. 3 plots SCR statistics from simulations against those predicted by multiple linear regression. Six toolpaths with the same number of L-turns are highlighted to demonstrate the range of the toolpath enumeration process. Spiral-like toolpaths, dominated by L-turns and parallel track pairs, tend to have higher SCR mean, and therefore finer grain sizes, than serpentine-like toolpaths, dominated by U-turns and antiparallel track pairs. Toolpaths that are neither spiral or serpentine have unique mechanical properties (such as anisotropy and residual stress) and can be easily substituted into island strategies or for complex microstructural designs.

5. Conclusions and future works

Expanding the toolpath design space improves AM parameter optimization. We present a method for enumerating AM toolpaths on discreditable geometries and characterizing irregular toolpaths by their internal structures. Even if all builds have same global AM parameters and global energy density (GED), variations in toolpath internal structures produce variations in cooling rates, allowing for new possibilities for microstructural design. Future work includes generalization of this method to larger geometries and more complex characterization of internal structures. The interaction between different internal structures should also be studied.

Declaration of Competing Interest

The authors declare that they have no known competing financial interests or personal relationships that could have appeared to influence the work reported in this paper.

Acknowledgments

The authors acknowledge support by the National Institute of Standards and Technology (NIST) – Center for Hierarchical Material Design (ChiMaD) under grant No. 70NANB14H012 and the National Science Foundation (NSF) – Cyber-Physical Systems (CPS) under grant No. CPS/CMMI-1646592. The authors would also like to thank Stephen Lin and Kevontrez Jones from Northwestern University for providing technical expertise on thermal simulations.

Appendix A. Supplementary data

Supplementary data to this article can be found online at https://doi.org/10.1016/j.mfglet.2020.09.008.

References

[1] Gorsse S, Hutchinson C, Gouné M, Banerjee R. Additive manufacturing of metals: a brief review of the characteristic microstructures and properties of steels, Ti-6Al-4V and high-entropy alloys. Sci Technol Adv Mater 2017;18(1):584–610.
[2] Shamsaei N, Yadollahi A, Bian L, Thompson SM. An overview of Direct Laser Deposition for additive manufacturing; Part II: Mechanical behavior, process parameter optimization and control. Addit Manuf 2015;8:12–35.
[3] Wolff S, Lee T, Faierson E, Ehmann K, Cao J. Anisotropic properties of directed energy deposition (DED)-processed Ti–6Al–4V. J Manuf Process 2016;24:397–405.
[4] Nickel AH, Barnett DM, Prinz FB. Thermal stresses and deposition patterns in layered manufacturing. Mater Sci Eng A 2001;317(1–2):59–64.
[5] Mughal MP, Mufti RA, Fawad H. The mechanical effects of deposition patterns in welding-bflsed layered manufacturing. Proc Inst Mech Eng Part B J Eng Manuf 2007;221(10):1499–509.
[6] Catchpole-Smith S, Aboulkhair N, Parry L, Tuck C, Ashcroft IA, Clare A. Fractal scan strategies for selective laser melting of 'unweldable' nickel superalloys. Addit Manuf 2017;15:113–22.
[7] Ali H, Ghadbeigi H, Mumtaz K, Effect of scanning strategies on residual stress and mechanical properties of Selective Laser Melted Ti6Al4V, Mater Sci Eng A, 712, no. November 2017, pp. 175–187, 2018.
[8] Robinson J, Ashton I, Fox P, Jones E, Sutcliffe C. Determination of the effect of scan strategy on residual stress in laser powder bed fusion additive manufacturing. Addit Manuf 2018;23(July):13–24.
[9] Ding D, Pan Z, Cuiuri D, Li H. A tool-path generation strategy for wire and arc additive manufacturing. Int J Adv Manuf Technol 2014;73(1–4):173–83.
[10] Boissier M, Allaire G, Tournier C, Laser path optimization for additive manufacturing, 2019.
[11] Mohanty S, Hattel J. Cellular scanning strategy for selective laser melting: capturing thermal trends with a low-fidelity, pseudo-analytical model. Math Probl Eng 2014;2014.
[12] Zhang B, Li Y, Bai Q. Defect formation mechanisms in selective laser melting: a review, Chin J Mech Eng (English Edition), vol. 30, no. 3. Chinese Mechanical Engineering Society, pp. 515–527, 01-May-2017.
[13] Sloane NJA. The on-line encyclopedia of integer sequences (OEIS), sequence A096969. [Online]. <https://oeis.org/A096969>.
[14] Guo Q, Zhao C, Qu M, Xiong L, Escano L, Hojjatzadeh S, et al. In-situ characterization and quantification of melt pool variation under constant input energy density in laser powder bed fusion additive manufacturing process. Addit Manuf 2019;28:600–9.
[15] Hooper PA. Melt pool temperature and cooling rates in laser powder bed fusion. Addit Manuf 2018;22:548–59.
[16] Martin AA, Calta NP, Khairallah SA, Wang J, Depond PJ, Fong AY, et al. Dynamics of pore formation during laser powder bed fusion additive manufacturing. Nat Commun 2019;10(1):1–10.
[17] Chan HS, Dill KA. Compact polymers. Macromolecules 1989;22(12):4559–73.
[18] Oberdorf R, Ferguson A, Jacobsen JL, Kondev J. Secondary structures in long compact polymers. Phys Rev E - Stat Nonlinear, Soft Matter Phys 2006;74(5):1–14.
[19] He L, Ren X, Gao Q, Zhao X, Yao B, Chao Y. The connected-component labeling problem: a review of state-of-the-art algorithms. Pattern Recognit 2017;70:25–43.
[20] Bradski G. The Opencv Library, vol. 25. 2000.
[21] Fujishima M, Oda Y, Ashida R, Takezawa K, Kondo M. Study on factors for pores and cladding shape in the deposition processes of Inconel 625 by the directed energy deposition (DED) method. CIRP J Manuf Sci Technol 2017;19:200–4.
[22] Gan Z, Lian Y, Lin SE, Jones KK, Liu WK, Wagner GJ. Benchmark study of thermal behavior, surface topography, and dendritic microstructure in selective laser melting of Inconel 625. Integr Mater Manuf Innov 2019;8(2):178–93.
[23] Wolff SJ, Lin S, Faierson EJ, Liu WK, Wagner GJ, Cao J. A framework to link localized cooling and properties of directed energy deposition (DED)-processed Ti-6Al-4V. Acta Mater 2017;132:106–17.
[24] Zheng B, Zhou Y, Smugeresky JE, Schoenung JM, Lavernia EJ. Thermal behavior and microstructure evolution during laser deposition with laser-engineered net shaping: Part II. Experimental investigation and discussion. Metall Mater Trans A Phys Metall Mater Sci 2008;39(9):2237–45.
[25] Farshidianfar MH, Khajepour A, Gerlich AP. Effect of real-time cooling rate on microstructure in Laser Additive Manufacturing. J Mater Process Technol 2016;231:468–78.
[26] Fotovvati B, Wayne SF, Lewis G, Asadi E, A review on melt-pool characteristics in laser welding of metals, Adv Mater Sci Eng, 2018. Hindawi Limited, 2018.